

https://doi.org/10.1070/QEL17982

Study of *t*-ZrO_2:Eu^{3+} nanophosphor obtained by laser vaporisation using a cw CO_2 laser

A.I. Kostyukov, A.A. Nashivochnikov, Vl.N. Snytnikov, M.I. Rakhmanova, V.N. Snytnikov

Abstract. **ZrO_2:Eu^{3+} nanophosphor has been fabricated by vaporisation of a ceramic target of specified composition using a CO_2 laser, with subsequent vapour condensation in an argon flow. Nanoparticles with spherical morphology have been synthesised at a pressure of 0.1 atm. The *t*-ZrO_2 phase is found to be dominant (98%). According to the transmission electron microscopy data, the nanoparticle size is 10 ± 4 nm. The luminescence properties of fabricated nanoparticles have been studied. It is shown that the strong red luminescence of the samples is mainly due to the bands peaking at 591 and 606 nm, which are related, respectively, to the $^5D_0 \rightarrow {}^7F_1$ and $^5D_0 \rightarrow {}^7F_2$ transitions of Eu^{3+} ion in the *t*-ZrO_2 structure. It is shown also that europium is uniformly distributed over the ZrO_2 matrix during laser synthesis. A comparative study of the *t*-ZrO_2:Eu^{3+} nanophosphor and the initial coarse-grained target has been performed. It is concluded that the proposed method of laser vaporisation is promising for synthesising *t*-ZrO_2-based nanophosphors.**

Keywords: *laser vaporisation, CO_2 laser, phosphor, nanoparticles, t-ZrO_2, Eu^{3+} luminescence.*

1. Introduction

The fabrication of functional oxide nanomaterials with controlled elemental and phase compositions is one of key problems of nanotechnologies [1]. Laser methods for fabricating nanomaterials have been actively elaborated in recent years to solve this problem. The main methods of laser synthesis of oxide nanoparticles are laser gas-phase evaporation [2–8] and laser ablation (with plasma generation), including the actively developing method of pulsed laser ablation in liquid [9–14]. An advantage of laser methods is the possibility of controlling many synthesis parameters, such as laser characteristics, composition and pressure of buffer gas during vaporisation and its circulation velocity, initial characteristics of powders, and configuration of the vaporisation chamber; all these parameters affect the physicochemical properties of synthesised nanoparticles. Thus, this approach allows one to vary controllably the particle size, composition, stoichiometry, and size distribution. The size of nanoparticles fabricated by laser vaporisation is controlled mainly by changing the buffer gas composition and pressure in the vaporisation chamber [1–8]. For example, particles of smaller size can be formed using a buffer gas of lower molecular weight (e.g., He instead of Ar) or reducing its pressure in the vaporisation chamber. Laser vaporisation with controlled vapour condensation is an efficient method for fabricating nanomaterials of different types, including metals, alloys, metal oxides, and semiconductors [1–14]. Laser synthesis methods are actively applied to produce simple oxides, for example, Al_2O_3, ZrO_2, TiO_2, Y_2O_3, Gd_2O_3, and SiO_2, as well as multicomponent compounds on their basis [3–6, 15–19]. The radiation sources generally used for laser synthesis are cw and pulsed-periodic CO_2 lasers [2–7], Nd:YAG laser (in particular, its second harmonic at 532 nm) [8, 18], and fiber lasers [19]. As was reported in [7], the use of laser radiation with short pulses (10^{-8} s or shorter) and low average output power is limited because of very low nanoparticle production output. To date, CO_2 lasers are the most widespread sources all over the world; being highly universal in comparison with other lasers [20], they are widely used to produce nanomaterials. The radiation of a cw CO_2 laser of moderate power (to 100 W), used in this study, allows one to obtain nanoparticles with a narrow size distribution in the evaporative regime, without plasma formation [21]. In this regime the nanoparticle formation output exceeds that obtained in the ablation regime with plasma formation [14].

Zirconium dioxide (ZrO_2) is of great interest from both scientific and technological points of view. ZrO_2 is characterised by high thermal and chemical stability. It is also highly transparent and, correspondingly, promising as a matrix for luminescent materials. Trivalent europium is widely applied as an activator in such phosphors because of its intense red luminescence and ability to play the role of a luminescence probe when studying a local structure of the material. The luminescence spectrum of Eu^{3+} consists generally of bands that are due to the intraconfiguration 4f–4f transitions $^5D_0 \rightarrow {}^7F_J$. Materials based on the tetragonal (*t*) phase of zirconia are in great demand as optical ceramics and phosphors. However, it is the monoclinic ZrO_2 phase that is stable at room temperature and up to 1170 °C. Nevertheless, the *t* phase at room temperature can also be stabilised by introducing Eu^{3+} cations into the ZrO_2 structure.

A.I. Kostyukov, A.A. Nashivochnikov Novosibirsk State University, ul. Pirogova 1, 630090 Novosibirsk, Russia; Boreskov Institute of Catalysis, Siberian Branch, Russian Academy of Sciences, prosp. Akad. Lavrent'eva 5, 630090 Novosibirsk, Russia;
e-mail: ant.kostyukov@mail.ru, mataiassaiatam17@gmail.ru;
Vl.N. Snytnikov, V.N. Snytnikov Boreskov Institute of Catalysis, Siberian Branch, Russian Academy of Sciences, prosp. Akad. Lavrent'eva 5, 630090 Novosibirsk, Russia;
e-mail: vn-snyt@mail.ru, snyt@catalysis.ru;
M.I. Rakhmanova Nikolaev Institute of Inorganic Chemistry, Siberian Branch, Russian Academy of Sciences, prosp. Akad. Lavrent'eva 3, 630090 Novosibirsk, Russia; e-mail: rakhmanova_m@mail.ru

Received 19 October 2021
Kvantovaya Elektronika **52** (2) 149–154 (2022)
Translated by Yu.P. Sin'kov

The use of laser methods for fabricating ZrO_2 and YSZ nanoparticles was described in several studies [3, 22–26]. At the same time, as far as we know, there are no studies on purposeful synthesis of t-$ZrO_2:Eu^{3+}$ phosphor by these methods. However, according to the data in the literature, efficient methods for fabricating this phosphor are in constant demand [27, 28]. Our purpose was to fabricate a t-$ZrO_2:Eu^{3+}$ nanophosphor by laser vaporisation using an original experimental setup and study the characteristics of the obtained nanopowders.

2. Experimental

2.1. Fabrication of t-$ZrO_2:Eu^{3+}$ nanophosphor

$ZrO_2:Eu^{3+}$ nanoparticles were obtained in two stages. First, microcrystalline powder $ZrO_2:Eu^{3+}$ was prepared. Then it was pressed into pellets: targets for vaporisation (Fig. 1b). Powders were produced based on the classical incipient wetness impregnation method of initial $ZrOCl_2 \cdot 8H_2O$ (of reagent grade) by aqueous solutions of nitric europium $Eu(NO_3)_3 \cdot 6H_2O$ (of reagent grade). A preliminary prepared aqueous solution of $Eu(NO_3)_3 \cdot 6H_2O$ with a specified europium concentration was added drop by drop to the $ZrOCl_2 \cdot 8H_2O$ powder. The impregnated samples were then dried at 110 °C for 4 h with subsequent high-temperature heat treatment at 1200 °C for 6 h (heating to 1200 °C was performed at a rate of 100 °C per hour). After this treatment, the samples were pressed in an evacuated mold under a load of 13 t into pellets 18 mm in diameter. Before the vaporisation the pellets were additionally annealed at 1200 °C for 4 h to improve their strength characteristics. The target density was 4.3–4.4 g cm^{-3}. The phase and chemical composition of targets in all preparation stages was monitored by X-ray diffraction (XRD) and X-ray fluorescence analysis.

In the second stage, $ZrO_2:Eu^{3+}$ nanopowder was produced in a two-chamber laser vaporisation setup (Fig. 1a).

The setup consists of an external sealed steel chamber (*9*) of volume 16 L, with operating pressures ranging from 0.1 Pa to 200 kPa; a vacuum post (*20*); systems of laser beam input (*1–8*) and optical monitoring; and systems for moving a crucible with target (*14*) and for feeding gases and monitoring pressure in the chamber, (*17–19, 21*). Targets were evaporated from a crucible (*15*), made of stainless steel 12Kh18N9T, in a vaporisation chamber (*10*) with a labyrinthine scheme of particle separation (*11*) in a gas flow. Particles captured by the flow were deposited on ash-free paper filters 110 mm in diameter (*16*), separating the vaporisation chamber from the vacuum pumping channel. The vaporisation was monitored visually, using a transparent glass window of the external chamber, through the cylindrical quartz housing of an internal chamber (*12*).

Vaporisation occurred when the cw CO_2 laser beam was focused on the target into a spot 0.4–0.5 mm in diameter, where a boiling zone with a temperature of 4000–4300 °C and a melt zone 2–3 mm in diameter with a temperature of

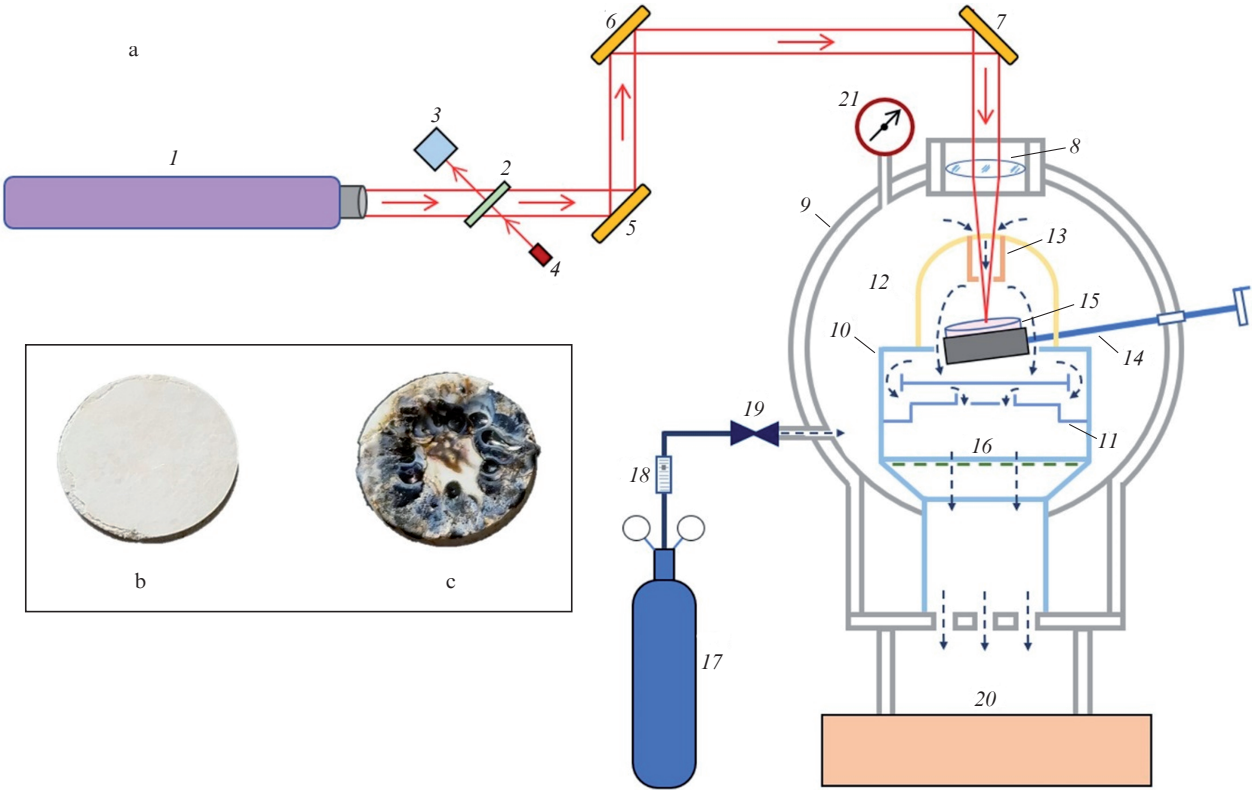

Figure 1. (Colour online) (a) Schematic of the experimental setup for fabricating $ZrO_2:Eu^{3+}$ nanopowder:
(*1*) cw CO_2 laser; (*2*) beam splitter; (3) radiation power meter; (*4*) tracing semiconductor laser; (*5–7*) optical path mirrors; (*8*) objective; (*9*) external vacuum chamber; (*10*) vaporisation chamber; (*11*) labyrinthine gas circulation system; (*12*) internal chamber quartz housing; (*13*) nozzle head; (*14*) rod for crucible fixing and target scanning; (*15*) target in crucible; (*16*) paper filter; (*17*) balloon with gas; (*18*) rotameter; (*19*) valve; (*20*) vacuum post; (*21*) pressure gauge; solid red arrows indicate the laser beam propagation direction, and dashed arrows show the gas flow motion direction. (b, c) Target photographs prior to vaporisation (b) and after laser irradiation in the vaporisation chamber (c).

2500–2700 °C were formed. The hand-made laser in use had the following characteristics: radiation wavelength of 10.6 μm, radiation power of up to 120 W in one transverse mode TEM_{00}, output beam diameter of 8 mm, and divergence of 3 mrad in the far-field zone. In all experiments on ZrO_2:Eu^{3+} nanopowder production the output laser power was 100 W. The radiation power was monitored using a calibrated scheme, including a ZnSe beam splitter (*2*) with an antireflection coating and an LM-2 power meter (*3*) (Karl Zeiss Jena). To ensure uniform vaporisation, the crucible with a target was moved relative to the laser beam by rotating a rod with its simultaneous displacement along the rotation axis. A photograph of the target after laser irradiation in the vaporisation chamber is shown in Fig. 1c. It can be seen that the colour of a target processed by intense laser beam changes in the irradiated region; this change is caused by burning oxygen out of ZrO_2.

Cooling and condensation of the vapour of oxides and their radicals were performed in a flow of high-purity (99.998%) buffer gas Ar, fed through a nozzle (*13*), coaxial with the laser beam. Nanoparticle deposition occurred throughout the entire vaporisation channel along the gas and dust flow propagation direction. The vaporisation chamber was designed so as to make most of nanoparticles deposit on a filter. The vaporisation experiments were performed at a characteristic pressure of 10 kPa (0.1 atm). To preserve a narrow size distribution of produced nanoparticles, the pressure in the chamber was maintained constant during the entire synthesis cycle. Previously the chamber with a target was sealed and evacuated by a backing pump to a residual pressure of 0.02 Pa. The typical Ar consumption rate was 130 normal L h^{-1}.

The vaporisation of a laser-irradiated ceramic target is accompanied by the formation of micrometer fragments and melt spray. To prevent large particles from entering the final nanopowder, the system in use was equipped with a labyrinthine gas circulation scheme on the path from the vaporisation zone to the filter, on which nanoparticles with the narrowest size distribution were deposited. As showed a transmission electron microscopy (TEM) study of the ZrO_2:Eu^{3+} nanoparticles collected from different parts of the chamber, the labyrinthine system efficiently separated large particles from the nanopowder.

After cooling the chamber to room temperature and depressurisation, the nanopowder was collected, and its mass was measured on an electronic balance. The thus prepared samples were investigated by physicochemical methods.

2.2. Methods for study

An elemental analysis of the prepared phosphor was performed by the X-ray spectroscopic fluorescent method using an ARL Advant'X analyser with an Rh-anode X-ray tube. TEM micrographs were recorded using a Themis-Z 3.1 microscope (TFS), equipped with an X-FEG monochromator and a CS/S double corrector at an accelerating voltage of 200 kV. An elemental analysis was performed using a Super-X EDS detector (energy resolution of about 120 eV) in the HAADF-STEM regime. Samples for TEM analysis were prepared by ultrasonic dispersion in ethanol with subsequent deposition of suspension on a 'perforated' carbon film, fixed on copper meshes. The phase compositions of the initial powder and prepared nanophosphor were determined by XRD using a D8 diffractometer (Bruker) (Cu K_α radiation, $\lambda = 1.5418$ Å). The luminescence properties of the samples were studied using a Fluorolog-3 spectrofluorimeter (Horiba Jobin Yvon). This instrument is a modular system based on double monochromators (Czerny–Turner configuration) with a flat diffraction grating and a xenon lamp with radiation power of 450 W serving as a luminescence excitation source. The radiation detector was a photoelectron multiplier, sensitive in the range of 200–850 nm. Luminescence spectra were recorded at room temperature with a resolution of 0.5 nm. The recorded spectra were corrected using standard correction curves.

3. Experimental results and discussion

Under given conditions, the characteristic values of laser synthesis output for the ZrO_2:Eu^{3+} sample collected over the entire vaporisation channel were 1.2 g h^{-1}. The fraction of the particles with the narrowest size distribution, deposited on the filter, was no less than 52%.

After the vaporisation of initial ceramic ZrO_2:Eu^{3+} targets, the sample morphology changed significantly. According to the TEM data, the powder obtained in this way consists of weakly agglomerated nanoparticles with a shape close to spherical (Fig. 2). An approximation by a lognormal distribution showed the average particle diameter to be 10 ± 4 nm. To plot a size distribution, we measured the diameter of more

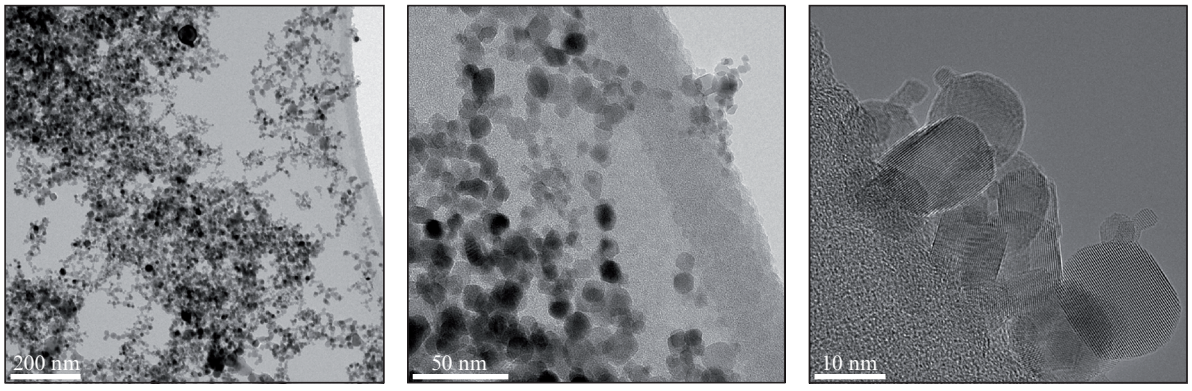

Figure 2. TEM images (with different magnifications) of ZrO_2:Eu^{3+} nanoparticles obtained by laser vaporisation.

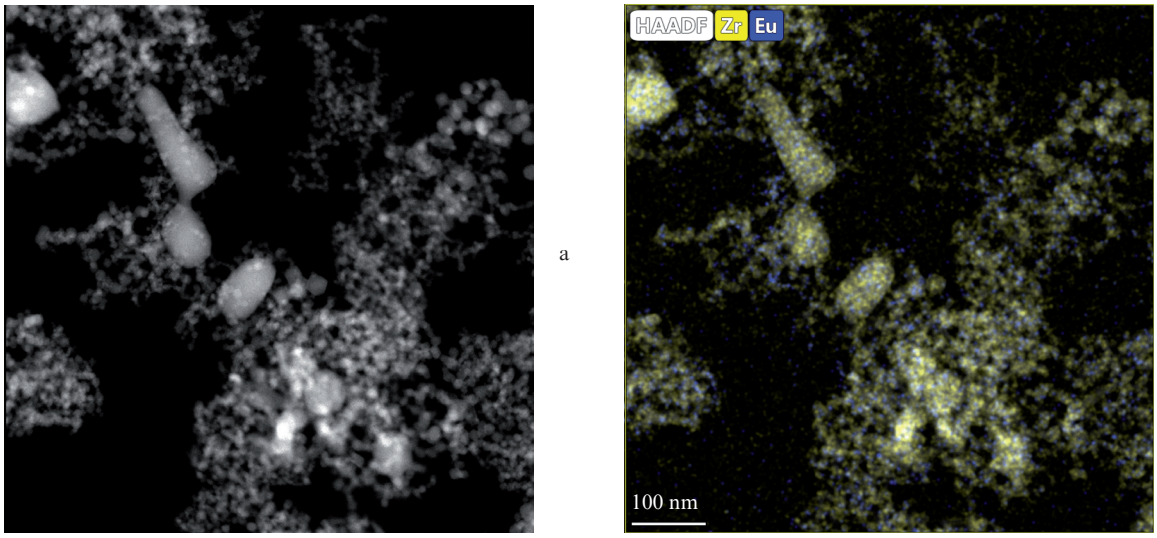

Figure 3. (Colour online) (a) HAADF-STEM image of a region containing $ZrO_2:Eu^{3+}$ nanoparticles and (b) EDS map of zirconium and europium distribution for this region.

than 700 nanoparticles. It can be seen that the size distribution of laser-synthesised nanoparticles is rather narrow. The fraction of particles with sizes from 50 to 100 nm is no more than 1%. This fact indicates that the nanomaterial fabrication technology proposed here is efficient for fabricating nanoparticles with a narrow size distribution.

Figure 3 shows an HAADF-STEM image of a fragment of $ZrO_2:Eu^{3+}$ nanopowder and the corresponding elemental distribution map of europium and zirconium. After the laser vaporisation the europium concentration in the sample was 6.85 wt %. It can be seen that europium is uniformly distributed over the ZrO_2 matrix.

Figure 4 shows an XRD pattern of the initial (before pelletisation) $ZrO_2:Eu^{3+}$ micropowder and the $ZrO_2:Eu^{3+}$ nanopowder fabricated by laser vaporisation. To identify the phase composition of the samples, Fig. 4 shows also standard XRD patterns for monoclinic, tetragonal, and cubic modifications of ZrO_2.

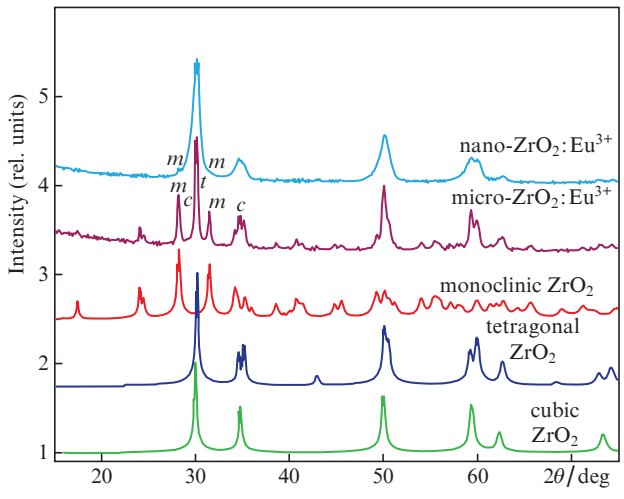

Figure 4. (Colour online) Diffraction patterns of the initial $ZrO_2:Eu^{3+}$ micropowder and $ZrO_2:Eu^{3+}$ nanopowder obtained by laser vaporisation, supplemented with standard ICSD data on the monoclinic (*m*, PDF 010-83-0939), tetragonal (*t*, PDF 010-70-6627), and cubic (*c*, PDF 010-70-6632) modifications of ZrO_2.

The diffraction patterns of the initial $ZrO_2:Eu^{3+}$ micropowder contain peaks characteristic of three ZrO_2 modifications. The monoclinic, tetragonal, and cubic phases in the sample were in a ratio of 48:39:13. The presence of tetragonal phase is indicated by the peak at $2\theta = 30.1°$. Note also that this peak is asymmetric because of the peak located at $2\theta = 29.9°$, which is due to the cubic phase. The occurrence of the peak at $2\theta = 34.7°$ indicates more clearly to the formation of cubic phase. The lattice parameters for each phase found in the sample are as follows: $a = 5.155(1)$ Å, $b = 5.208(1)$ Å, $c = 5.316(1)$ Å, $\beta = 99.12(1)°$ for the monoclinic phase; $a = 3.612(1)$ Å and $c = 5.186(1)$ Å for the tetragonal phase; and $a = 5.160(1)$ Å for the cubic phase. After evaporating the target prepared from this sample, the structure of ready nanoparticles changed significantly. In this case, laser vaporisation provides conditions leading to stabilisation of mainly tetragonal phase. The presence of additional Eu^{3+} impurities even more facilitates stabilisation. For example, according to the XRD data, the phase composition of $ZrO_2:Eu^{3+}$ nanopowders exhibits dominance of the tetragonal phase: its content is 98% (see Fig. 4). The lattice parameters for this phase are as follows: $a = 3.608(4)$ Å and $c = 5.184(1)$ Å. The rest (2%) is the ZrO_2 monoclinic phase. The average nanoparticle size, found from the coherent-scattering region (CSR) for the tetragonal phase, is ~9 nm, which is in good correspondence with the TEM data.

The luminescence characteristics of the initial powder and the t-$ZrO_2:Eu^{3+}$ nanophosphor prepared from it were studied under direct excitation near the $^7F_0 \rightarrow {}^5L_6$ transition of Eu^{3+} ions with $\lambda_{max} = 395$ nm (Fig. 5).

It can be seen in Fig. 5 that the luminescence spectrum of the initial polycrystalline $ZrO_2:Eu^{3+}$ powder contains groups of bands in the ranges of 580–583, 584–602, 602–638, 644–667, and 692–721 nm, which are due to the electronic transitions $^5D_0 \rightarrow {}^7F_J$ (J = 0–4) of Eu^{3+} ions. The complex

structure of the fluorescence spectrum of the initial powder is related to the luminescence of Eu^{3+} ions existing simultaneously in several ZrO_2 phases. A significant contribution to the spectrum is from the Eu^{3+} ions in the monoclinic phase structure. For example, the luminescence spectrum contains a band due to the $^5D_0 \rightarrow {}^7F_0$ transition (forbidden by all selection rules), peaking at 582 nm, as well as series of bands due to the $^5D_0 \rightarrow {}^7F_J$ transitions (J = 0–4). The structure of these transitions contains 3, 5, 7, and 9 components, respectively, which means complete removal of degeneracy of the ^7F_J levels. The strongest luminescence bands, with maxima at 590, 597, 598.5 nm and 614, 615, 617, 625, 632 nm, are due to the $^5D_0 \rightarrow {}^7F_1$ and $^5D_0 \rightarrow {}^7F_2$ transitions, respectively. Splitting of the ^7F_J levels of Eu^{3+} in the crystalline field into as many as possible components indicates that europium occupies a site with low local symmetry (C_1, C_2, or C_s) in the ZrO_2 monoclinic phase, which is in good agreement with the data in the literature [29–32]. The luminescence spectra also demonstrate a significant content of tetragonal ZrO_2 phase in the initial sample. For example, there are additional bands peaking at 592, 595 and 607, 635 nm in the spectrum, which are

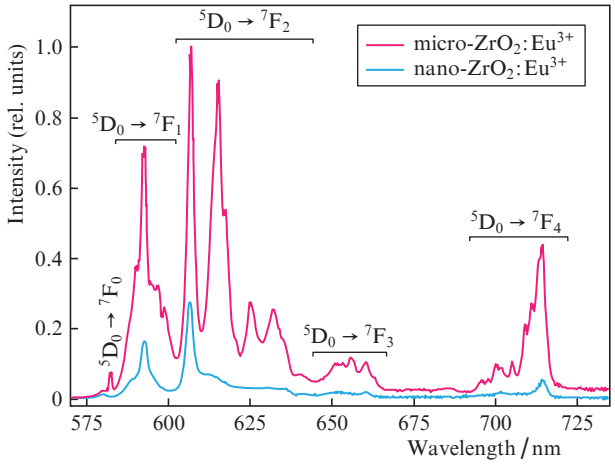

Figure 5. (Colour online) Luminescence spectra of the initial and nanosized ZrO_2:Eu^{3+} powders (λ_{exc} = 395 nm).

due to the $^5D_0 \rightarrow {}^7F_1$ and $^5D_0 \rightarrow {}^7F_2$ transitions of Eu^{3+} ions in the t-ZrO_2 structure. Based on the analysis of the band structure, it was concluded that Eu^{3+} ions in the t-ZrO_2:Eu^{3+} matrix are incorporated into sites with local symmetry D_{2d}.

According to the XRD data, significant changes occur in the sample structure after vaporisation, as can be seen well in the luminescence spectra. In contrast to the spectra of the initial sample, bands with maxima at 591 and 606 nm dominate in the luminescence spectra of t-ZrO_2:Eu^{3+} nanopowder; these bands are due to the $^5D_0 \rightarrow {}^7F_1$ and $^5D_0 \rightarrow {}^7F_2$ transitions of Eu^{3+} ions, respectively. The weaker bands in the spectra may be due to the presence of Eu^{3+} in the ZrO_2 monoclinic phase, which is in agreement with the XRD data. One can also see in Fig. 5 that the spectra of the sample obtained by laser vaporisation exhibit inhomogeneous line broadening, which is characteristic of nanosystems. The total Eu^{3+} luminescence intensity of the initial samples is much higher than that of the obtained nanopowder. Nanoparticles have larger specific surface areas in comparison with coarse-grained samples. Various molecules, OH and CO_x groups adsorb from atmosphere on a highly developed surface. Therefore, the lower luminescence intensity of nanopowders is generally explained by the higher probability of nonradiative processes because of the interaction with the OH and CO_x groups adsorbed on the surface. Another, more important reason in the case of ZrO_2 is the formation of oxygen vacancies in the structure of europium-doped ZrO_2 because of the difference in the charge states of Zr^{4+} and Eu^{3+} ions. Detailed explanation of the aforementioned decrease in the luminescence intensity is beyond the scope of this study.

4. Conclusions

Europium-doped ZrO_2 nanophosphor with a concentration of 6.85 wt % was obtained by laser vaporisation of a polycrystalline target of specified chemical composition in a buffer gas flow. The radiation source was a cw CO_2 laser with output power of 100 W. Target vaporisation and subsequent vapour condensation were performed in an argon gas flow at a pressure of 0.1 atm in the vaporisation chamber. These synthesis conditions provided weakly agglomerated nanopowders of ZrO_2:Eu^{3+} phosphor with spherically symmetric particle morphology. The average nanoparticle size was estimated from the TEM data and CSR (XRD analysis) to be 10 ± 4 nm. It also follows from the XRD data that the phase composition of nanoparticles is presented mainly by the t-ZrO_2 modification (98 %). High-resolution TEM and energy-dispersive X-ray analysis showed that europium is uniformly distributed over the t-ZrO_2 matrix in the nanopowders obtained by laser synthesis on the original setup presented in the paper. The luminescence spectra of the produced nanoparticles in the luminescence range of intraconfiguration transitions of Eu^{3+} were studied. It was shown that the intense red luminescence of the samples is mainly due to the bands peaking at 591 and 606 nm, which are related, respectively, to the $^5D_0 \rightarrow {}^7F_1$ and $^5D_0 \rightarrow {}^7F_2$ transitions of Eu^{3+} ion in the t-ZrO_2 structure.

The results of comparative structural and photoluminescence studies of the obtained t-ZrO_2:Eu^{3+} nanophosphor and initial polycrystalline powder (target material) are presented. Based on the analysis of the dataset on the structure, morphology, and luminescence properties, it was concluded that the proposed laser method has good prospects for fabricating t-ZrO_2-based nanophosphors.

Acknowledgements. TEM studies were performed using equipment of the Centre of Collective Use "National Centre of Catalyst Research". We are grateful to A.V. Ishchenko for carrying out the TEM analysis. The work was supported in part by the Ministry of Science and Higher Education of the Russian Federation, Project No. 1210317003138 (M.I. Rakhmanova) and the Russian Foundation for Basic Research, Project No. 19-32-60027 (A.I. Kostyukov).

References

1. Gusev A.I. *Nanomaterialy, nanostruktury, nanotekhnologii* (*Nanomaterials, Nanostructures, and Nanotechnologies*) (Moscow: Fizmatlit, 2009)
2. Wenisch C., Kurland H.D., Grabow J., Muller F.A. *J. Am. Ceram. Soc.*, **99**, 2561 (2016).
3. Kurland H.D., Grabow J., Muller F.A. *J. Eur. Ceram. Soc.*, **31**, 2559 (2011).
4. Kostyukov A.I., Snytnikov V.N., Yelisseyev A.P., Zhuzhgov A.V., Kostyukova N.Y., Ishchenko A.V., Cherepanova S.V., Snytnikov V.N. *Adv. Powder Technol.*, **32**, 2733 (2021).
5. Kostyukov A.I., Snytnikov V.N., Zhuzhgov A.V., Cherepanova S.V., Ishchenko A.V., Baronskiy M.G., Snytnikov V.N. *J. Alloys Compd.*, **815**, 152476 (2020).

6. Kostyukov A.I., Baronskiy M.G., Larina T.V., Snytnikov V.N., Zaitseva N.A., Pochtar A.A., Ishchenko A.V., Cherepanova S.V., Snytnikov V.N. *Mater. Charact.*, **169**, 110664 (2020).
7. Osipov V.V., Lisenkov V.V., Platonov V.V. *Pis'ma Zh. Tekh. Fiz.*, **37**, 103 (2011).
8. Bobb J.A., Awad F.S., Moussa S., El-Shall M.S. *J. Mater. Sci.*, **55**, 5351 (2020).
9. Kuz'min P.G., Shafeev G.A., Voronov V.V., Raspopov R.V., Arianova E.A., Trushina E.N., Gmoshinskii I.V., Khotimchenko S.A. *Quantum Electron.*, **42** (11), 1042 (2012) [*Kvantovaya Elektron.*, **42** (11), 1042 (2012)].
10. Bulgakov A.V., Evtushenko A.B., Shukhov Yu.G., Ozerov I., Marin V. *Quantum Electron.*, **40** (11), 1021 (2010) [*Kvantovaya Elektron.*, **40** (11), 1021 (2010)].
11. Miller J.C. *Mater. Sci.*, **28**, 56 (1994).
12. Lam J., Amans D., Chaput F., Diouf M., Ledoux G., Mary N., Masenelli-Varlot K., Motto-Ros V., Dujardin C. *Phys. Chem. Chem. Phys.*, **16**, 963 (2014).
13. Zeng H., Du X.-W., Singh S.C., Kulinich S.A., Yang S., He J., Cai W. *Adv. Funct. Mater.*, **22**, 1333 (2012).
14. Phipps C. *Laser Ablation and its Applications* (Boston: Springer, 2007).
15. Kurland H.-D., Stotzel C., Grabow J., Zink I., Muller E., Staupendahl G., Muller F.A. *J. Am. Ceram. Soc.*, **93** (5), 1282 (2010).
16. Kostyukov A.I., Snytnikov V.N., Snytnikov V.N., Ishchenko A.V., Rakhmanova M.I., Molokeev M.S., Krylov A.S., Aleksandrovsky A.S. *Opt. Mater.*, **104**, 109843 (2020).
17. Kostyukov A.I., Snytnikov V.N., Snytnikov V.N., Rakhmanova M.I., Kostyukova N.Y., Ishchenko A.V., Cherepanova S.V., Krylov A.S., Aleksandrovsky A.S. *J. Lumin.*, **235**, 118050 (2021).
18. El-Shall M.S., Slack W., Vann W., Kane D., Hanley D. *J. Phys. Chem.*, **98** (12), 3067 (1994).
19. Kotov Yu.A., Samatov O.M., Ivanov M.G., et al. *Fiz. Tverd. Tela*, **81** (5), 65 (2011).
20. Spreafico C., Russo D., Degl'Innocenti R. *J. Intell. Manufacturing* (2021); https://doi.org/10.1007/s10845-021-01809-9.
21. Snytnikov V.N., Snytnikov Vl.N., Dubov D.A., et al. *Prikl. Mekh. Tekh. Fiz.*, **48** (2), 172 (2007).
22. Bartolomé J.F., Smirnov A., Kurland H.-D., Grabow J., Müller F.A. *Sci. Rep.*, **6**, 20589 (2016).
23. Kurland H.-D., Grabow J., Stötzel Chr., Müller F.A. *J. Ceram. Sci. Technol.*, **5**, 275 (2014).
24. Lohbauer U., Wagner A., Belli R., Stoetzel C., Hilpert A., Kurland H.-D., Grabow J., Müller F.A. *Acta Biomater.*, **6**, 4539 (2010).
25. Williams G., Coles G.S.V. *J. Mater. Chem.*, **8** (7), 1657 (1998).
26. Eilers H., Tissue B.M. *Mater. Lett.*, **24**, 261 (1995).
27. Vidya Y.S., Anantharaju K.S., Nagabhushana H., Sharma S.C., Nagaswarupa H.P., et al. *Spectrochim. Acta, Part A*, **135**, 241 (2015).
28. Huangqing L., Lingling W., Shuguang C., Bingsuo Z., Zhiwei P. *Appl. Surf. Sci.*, **253**, 3872 (2007).
29. Marin R., Sponchia G., Zucchetta E., Riello P., De Portu G., Enrichi F., Benedetti A. *J. Am. Ceram. Soc.*, **96**, 2628 (2013).
30. Colbea C., Avram D., Cojocaru B., Negrea R., Ghica C., Kessler V.G., Seisenbaeva G.A., Parvulescu V.I., Tiseanu C. *Nanomaterials*, **8**, 988 (2018).
31. Moon B.K., Kwon I.M., Jeong J.H., Kim C.S., YiS. S., Kim P.S., Choi H., Kim J.H. *J. Lumin.*, **122**, 855 (2007).
32. Ivanova E.V., Kravets V.A., Orekhova K.N., Gusev G.A., Popova T.B., Yagovkina M.A., Bogdanova O.G., Burakov B.E., Zamoryanskaya M.V. *J. Alloys Compd.*, **808**, 151778 (2019).